ADVANCED FUNCTIONAL MATERIALS
www.afm-journal.de

$FeO_{0.7}F_{1.3}$/C Nanocomposite as a High-Capacity Cathode Material for Sodium-Ion Batteries

Yong-Ning Zhou, Mahsa Sina, Nathalie Pereira, Xiqian Yu, Glenn G. Amatucci, Xiao-Qing Yang, Frederic Cosandey,* and Kyung-Wan Nam**

Searching high capacity cathode materials is one of the most important fields of the research and development of sodium-ion batteries (SIBs). Here, we report a $FeO_{0.7}F_{1.3}$/C nanocomposite synthesized via a solution process as a new cathode material for SIBs. This material exhibits a high initial discharge capacity of 496 mAh g^{-1} in a sodium cell at 50 °C. From the 3rd to 50th cycle, the capacity fading is only 0.14% per cycle (from 388 mAh g^{-1} at 3rd the cycle to 360 mAh g^{-1} at the 50th cycle), demonstrating superior cyclability. A high energy density of 650 Wh kg^{-1} is obtained at the material level. The reaction mechanism studies of $FeO_{0.7}F_{1.3}$/C with sodium show a hybridized mechanism of both intercalation and conversion reaction.

1. Introduction

On account of the increasing concern of the limited lithium sources owing to the emerging large scale applications of lithium-ion batteries (LIBs), sodium-ion batteries (SIBs) are now attracting more and more attentions in energy storage society due to their low cost and abundance of sodium.[1] The major challenge in developing advanced SIBs is to find appropriate electrode materials with high capacity and good reversibility, which are extremely important for the performance of full cells.[2] Newly developed cathode materials for SIBs are mainly based on intercalation mechanism.[3] However, most of them show low reversible capacities (<180 mAh g^{-1}). From the scientific point of view, sodium intercalation is more challenging than lithium intercalation because the Na^+ ion has much larger (≈70%) ionic radius than the Li^+ ion, which results in high energy barrier for Na^+ ion insertion/extraction and structural degradation of the host during cycling.

In LIBs system, it is well known that high capacity can be achieved by utilizing materials based on conversion reactions, such as metal fluorides,[4] metal oxides[5] and metal nitrides,[6] which differ from the intercalation materials by their reaction mechanism. Among them, metal fluorides have been extensively studied as potential high capacity cathode materials due to their relatively high working potential and high capacity (500 to 750 mAh g^{-1}) versus lithium. Although the theoretical cell potential of metal fluorides versus sodium is 0.44 V lower than the lithium system,[7] this shortcoming can be compensated by their high capacity. Thus, it is valuable to examine the feasibility of conversion reactions based on metal fluorides in sodium ion system. Nishijima et al.[8] studied the electrochemical performance of FeF_3 versus Na but ended up with a low initial discharge capacity around 150 mAh g^{-1} and reversible capacity less than 100 mAh g^{-1} between 1.5 to 4.0 V vs Na^+/Na. Li et al.[9] synthesized a single wall carbon nanotubes (SWNTs) wired $FeF_3 \cdot 0.5H_2O$ electrode and tested its Na-storage property. It exhibited a reversible capacity of 100 mAh g^{-1}, and only 74 mAh g^{-1} were preserved after 50 cycles. Compared with the electrochemical performance of FeF_3 in LIBs system,[4b,4c] FeF_3 seems not to be fully active in SIBs system. Several other metal fluorides like TiF_3, MnF_3, and CoF_3 were also investigated for sodium storage, but all of them showed poor electrochemical performances.[8]

Previous research suggests that the addition of small amounts of oxygen into the fluoride structure is effective in improving the material's electronic conductivity and reversibility of (re)conversion reactions with lithium.[10] It could be expected that introducing oxygen into metal fluorides may weaken the average bonding strength between cations and anions, which then facilitates the reversible electrochemical reaction between the active material and sodium. However, to the best of our knowledge, there has been no published report on the electrochemical behavior of the metal oxyfluorides for sodium ion batteries.

Here, we report the first experimental results of the electrochemical Na activity of a nanocomposite of carbon and iron oxyfluoride ($FeO_{0.7}F_{1.3}$/C) which was synthesized via a solution based process. The nanocomposite delivers very high reversible Na storage capacity of ≈360 mAh g^{-1} even after 50 cycles. The origin of such high Na-storage capacity of the nanocomposite

Dr. Y.-N. Zhou, Dr. X. Yu, Dr. X.-Q. Yang
Department of Chemistry
Brookhaven National Laboratory
Upton, New York 11973, USA
E-mail: xyang@bnl.gov
M. Sina, Prof. F. Cosandey
Materials Science and Engineering
Rutgers University
Piscataway, New Jersey 08854, USA
E-mail: cosandey@rci.rutgers.edu
Dr. N. Pereira, Prof. G. G. Amatucci
Energy Storage Research Group (ESRG)
Rutgers University
North Brunswick, New Jersey 08902, USA
Prof. K.-W. Nam
Department of Energy and Materials Engineering
Dongguk University-Seoul
100715 Seoul, Republic of Korea
E-mail: knam@dongguk.edu

DOI: 10.1002/adfm.201403241

was systematically investigated and revealed by using a combination of synchrotron-based X-ray diffraction (XRD), X-ray absorption spectroscopy (XAS) and high-resolution transmission electron microscopy (HRTEM) with selected area electron diffraction (SAED) and electron energy loss spectroscopy (EELS) techniques.

2. Results and Discussions

2.1. Structure and Electrochemical Performance

Iron oxyfluoride (FeO_xF_{2-x}) is synthesized within x ranging from 0 to 1. It is found that when x is greater than 0.7, the FeO_xF_{2-x} compound synthesized in solution co-exists with Fe_2O_3 compounds, but remains single phase FeO_xF_{2-x} for x is equal and smaller than 0.7. Therefore, we investigated the sample with highest O content (x = 0.7) in single phase FeO_xF_{2-x} in order to maximize the effect of the oxygen substitution, which is considered to be beneficial by improving the material's electronic conductivity and electrochemical reversibility. **Figure 1**a shows the X-ray diffraction pattern of the $FeO_{0.7}F_{1.3}$/C nanocomposite. The broad diffraction peaks indicate the nanosize character of the materials. The average particle size was estimated to be about 15 nm by Scherrer equation using the (110) peak. All the diffraction peaks can be well indexed with a tetragonal rutile structure (Space group: $P4_2/mnm$). The lattice parameters of a = 4.668 Å and c = 3.076 Å were determined by the Le Bail fitting (Figure S1, Supporting Information). The value of 3.076 Å for parameter c implies the oxygen content x in the sample (FeO_xF_{2-x}) is around 0.7 based on the phase diagram established by Brink et al.[11] Figure 1b shows high-resolution TEM (HRTEM) image of the pristine $FeO_{0.7}F_{1.3}$/C nanocomposite. A well crystallized particle with a diameter of about 12 nm was observed. The lattice on the particle is attributed to (110) plane of rutile $FeO_{0.7}F_{1.3}$. The particle size distribution shown in Figure S2, Supporting Information, indicates the particle size of the pristine $FeO_{0.7}F_{1.3}$/C nanocomposite is in the range of 2–24 nm with a D50 value of 13 nm.

The galvanostatic charge and discharge tests of $FeO_{0.7}F_{1.3}$/C-Na cell were performed using 2032-coin cells at 50 °C. The cell was discharged to 1.0 V and then charged to 3.5 V versus sodium at a current density of 25 mA g^{-1} (based on the weight of $FeO_{0.7}F_{1.3}$) (**Figure 2**a). The initial discharge curve showed a continuous slope starting from the open circuit voltage (OCV), 2.4 V to about 1.5 V, followed by a plateau around 1.5 V. The initial discharge (i.e., sodiation) delivered a quite large capacity of 496 mAh g^{-1} corresponding to 1.7 Na per $FeO_{0.7}F_{1.3}$ (The theoretical capacity of $FeO_{0.7}F_{1.3}$ in SIBs is 787.7 mAh g^{-1} assuming full reduction of Fe ions to Fe^0.), which is comparable to the lithiation of $FeO_{0.7}F_{1.3}$ case in a lithium-ion system.[10a] The second discharge showed a capacity of 414 mAh g^{-1}, indicating relatively large capacity loss between the 1st and 2nd cycle. The shape of the discharge curves after the 2nd cycle is different from the initial discharge one. It could be attributed to the morphology and composition changes after the initial cycle. It is quite interesting to note that, after the 3rd cycle, a highly reversible capacity of 388 mAh g^{-1} is well preserved up to 50th cycles as shown in Figure 2b. The capacity fading mainly occurs

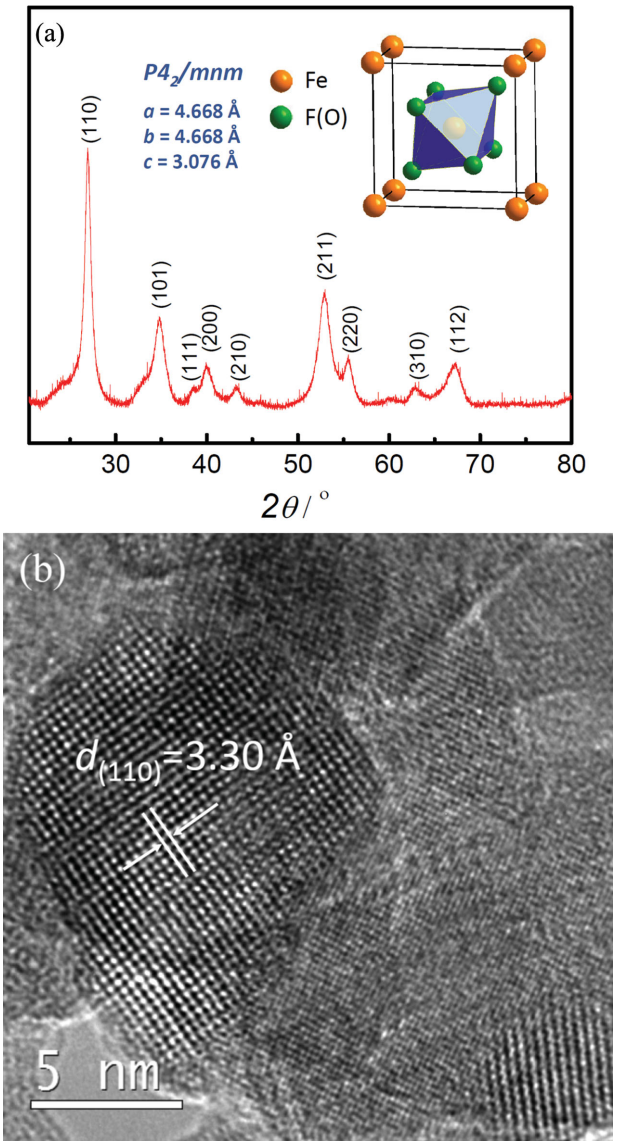

Figure 1. a) XRD patterns of the $FeO_{0.7}F_{1.3}$/C nanocomposite. b) HRTEM image of the pristine $FeO_{0.7}F_{1.3}$/C nanocomposite.

during the first three cycles while the capacity fading from 3rd to 50th cycles corresponds to only ≈0.14% per cycle. Indeed, the columbic efficiency maintains ≈99% after 50 cycles indicating superior Na-storage reversibility. After 50 cycles, a high Na storage capacity of 360 mAh g^{-1} can still be obtained. The discharge/charge curve of the 50th cycle is shown in Figure S3, Supporting Information. To the best of our knowledge, this is the highest reversible Na-storage capacity obtained in a cathode voltage range for sodium ion batteries.

The first two cyclic voltammograms of $FeO_{0.7}F_{1.3}$/C-Na cells between 1.0 and 3.5 V at a scan rate of 0.05 mV s^{-1} were shown in Figure 2c. In the first discharge process two broad peaks at around 1.7 V and 1.3 V were observed suggesting that two different reactions are involved during the initial sodiation process. Upon charge (i.e., desodiation), a major oxidation peak was seen in the 2.0–2.7 V region. In the second cycle, all of these reduction and oxidation peaks became

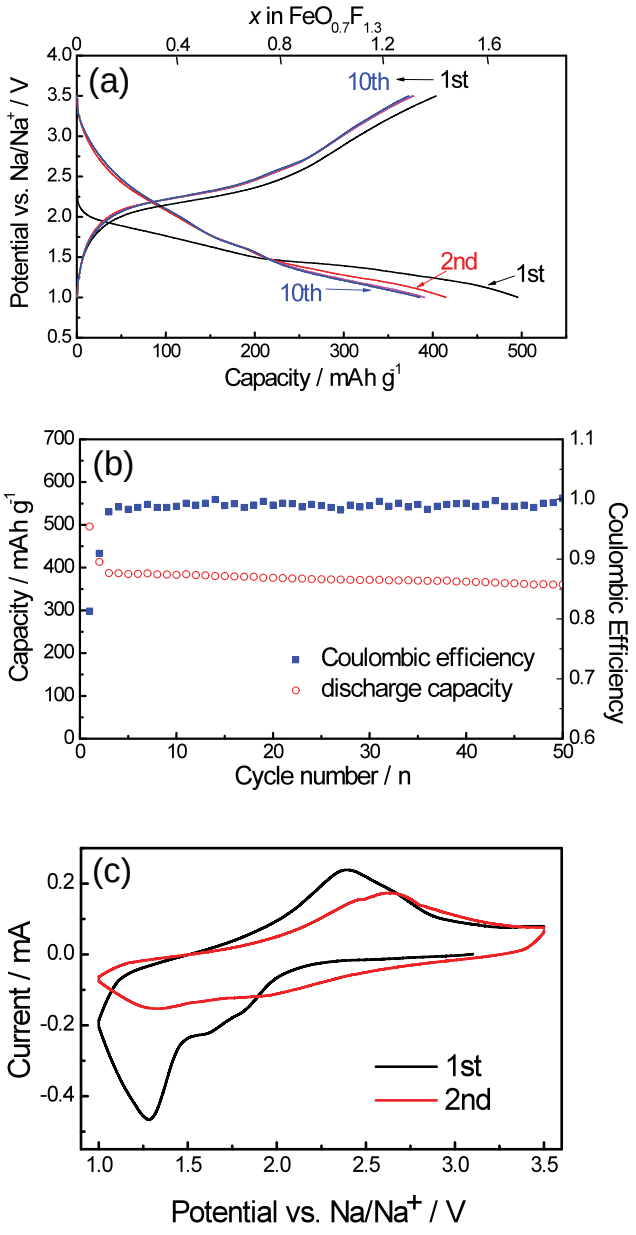

Figure 2. a) Discharge-charge profiles of the $FeO_{0.7}F_{1.3}$/C-Na cell between 1.0 and 3.5 V at a current density of 25 mA g^{-1} at 50 °C. b) Cycling performance of the $FeO_{0.7}F_{1.3}$/C-Na cell at a current density of 25 mA g^{-1} at 50 °C. c) The first two cyclic voltammograms of the $FeO_{0.7}F_{1.3}$/C-Na cells between 1.0 and 3.5 V at a scan rate of 0.05 mV s^{-1}.

broader with decreased intensity and shifted to higher potential slightly, which is in good agreement with the galvanostatic charge–discharge profiles.

2.2. Reaction Mechanism

2.2.1. X-Ray Absorption Spectroscopy (XAS) Characterization

To investigate the sodiation reaction mechanism of $FeO_{0.7}F_{1.3}$/C, in situ XAS at Fe K-edge during the 1st discharge was performed. The discharge curve and corresponding XAS scan number are shown in **Figure 3**a. As discussed above, the discharge curve can be divided into two parts (Region I and Region II) for a comprehensive comparison of the spectral feature changes. In Region I, a continuous voltage decline curve from 2.4 to 1.5 V was observed. The X-ray absorption near edge structure (XANES) spectra in Figure 3b show a rigid edge shift toward lower energy which manifests a continuous decrease in the average oxidation state of Fe. Average Fe oxidation state in the pristine $FeO_{0.7}F_{1.3}$ was estimated to be around +2.7 by comparing with the reference spectra of FeO (Fe^{2+}) and Fe_2O_3 (Fe^{3+}). At the end of Region I (Scan 26), the edge position shifted to the value close to Fe^{2+}. The charge compensation reaction of Fe estimated by XANES edge shift is in good agreement with the delivered capacity of about 210 mAh g^{-1} in Region I, which corresponds to 0.7 Na intercalated per $FeO_{0.7}F_{1.3}$. Figure 3c shows the XANES spectra in Region II. It can be seen that the white line of the spectrum does not shift but tilt during discharge. It indicates the chemical environment around Fe is changing dramatically. Based on the spectral feature changes in the XANES spectra, the sodiation reaction in Region II likely occurs through the conversion reaction. However, multi-phase reactions seem to be involved during this conversion reaction in Region II considering the absence of an isosbestic point in the XANES spectra.

Ex situ XAS are further measured at five different states during the initial discharge/charge cycle. The XANES spectra of each state shown in Figure 3d demonstrate that the features of two discharged spectra at 1.5 V and 1.0 V agree well with the XAS spectra measured in situ. The spectrum of the sample charged to 2.3 V shows an opposite tilting compared with the one discharged to 1.0 V. From 2.3 V to 3.5 V the absorption edge shifted back to higher energy, but the edge position was not completely recovered to its initial state. The average oxidation state of Fe after the 1st cycle was estimated to be about +2.4 based on the edge position. This value is 0.3 lower than that of pristine $FeO_{0.7}F_{1.3}$, which indicates that the charge–discharge process is not completely reversible, agreed well with the difference between the charge and discharge capacity for the initial cycle.

Figure 4a shows ex situ Fourier-transformed (FT) magnitudes of extended X-ray absorption fine structure (EXAFS) spectra at five different states in the first cycle of $FeO_{0.7}F_{1.3}$/C-Na cell. The first peak at $R \approx 1.5$ Å is due to the contribution from the nearest Fe-F/O6 octahedra in the rutile structure (marked as $R_{Ru}(1)$). The corresponding bond in the unit cell is shown in the Figure 4b. It should be noted that the FT peaks are not phase corrected, and thus the actual bond lengths are approximately 0.3–0.5 Å longer. The other two peaks at 2.7 and 3.3 Å are attributed to two different Fe–Fe bonds (marked as $R_{Ru}(2)$ and $R_{Ru}(3)$) in the rutile structure. During discharge process, the $R_{Ru}(1)$ peak shifts to higher value indicating the expansion of Fe-F/O_6 bond length. The decrease of the intensity of this peak, especially from 1.5 to 1.0 V, suggests the conversion reaction to metallic Fe phase at the expanse of the rutile phase. After discharge to 1.0 V, three new peaks at 2.3, 3.6, and 4.3 Å were observed corresponding to three different Fe-Fe distances in BCC metallic Fe phase (marked as $R_{Fe}(1)$, $R_{Fe}(2)$ and $R_{Fe}(3)$), which was formed through the conversion reaction. The other two remaining peaks at 1.7 and 2.9 Å could be assigned to a

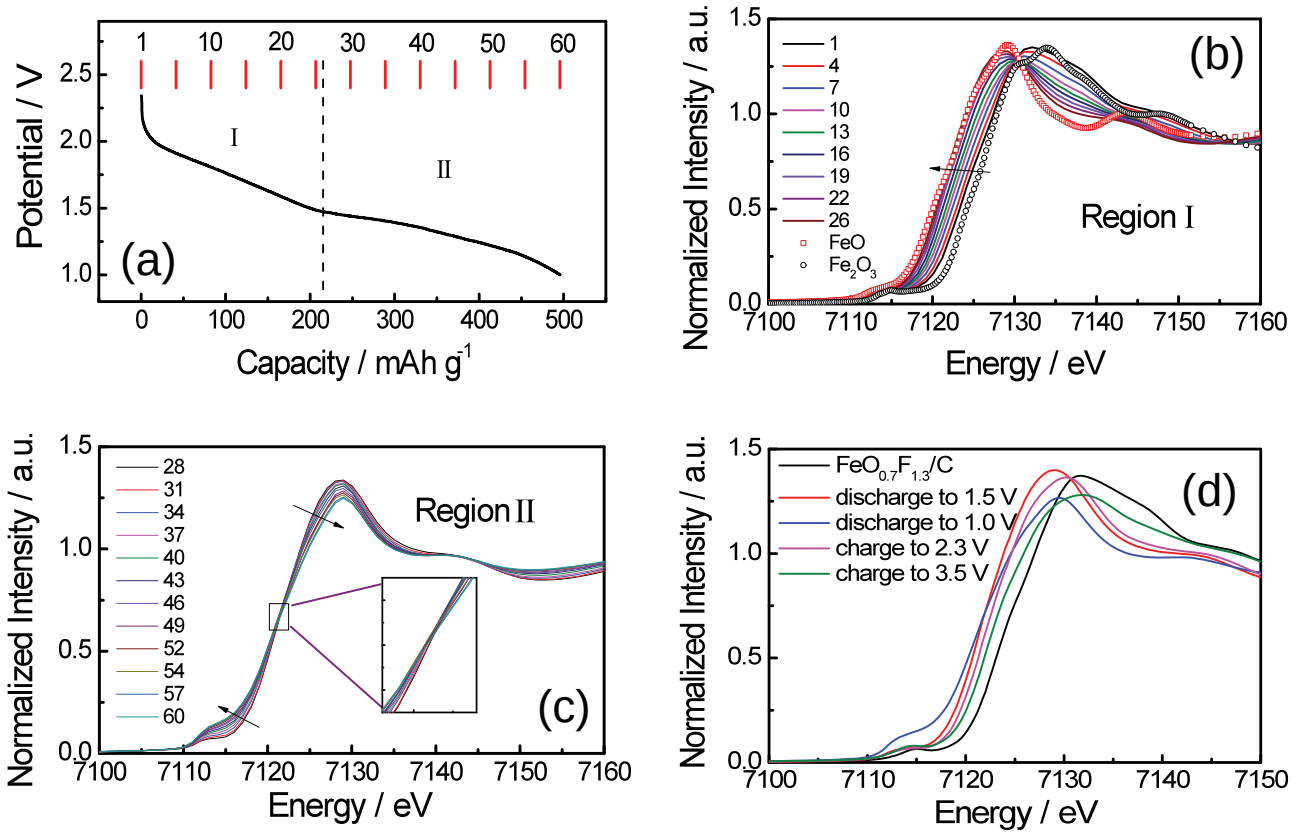

Figure 3. a) Initial discharge curve of the $FeO_{0.7}F_{1.3}$/C-Na cell during in situ XAS measurement. The numbers marked above the curve correspond to the scan numbers in XANES spectra. b,c) In situ Fe K-edge XANES spectra of the $FeO_{0.7}F_{1.3}$/C electrodes during the initial discharge for Region I and Region II, respectively. d) Ex situ Fe K-edge XANES spectra of the $FeO_{0.7}F_{1.3}$/C electrodes during the initial cycle.

new rutile phase with a larger Fe-F/O bond length or a rock salt phase. However it is difficult to distinguish them at this stage as their nearest two coordination spheres around Fe are very close to each other. After recharging back to 2.3 V, the peaks for metallic Fe disappeared and the other peaks shifted back to the position of a re-constructed rutile phase. When recharged to 3.5 V, the three peaks for the rutile structure almost recovered to the initial feature, indicating the reversible formation of rutile phase after one cycle. However, the relative peak intensity for $R_{Ru}(2)$ and $R_{Ru}(3)$ is different from that of the pristine material. From Figure 4b, we know that the coordination number of $R_{Ru}(2)$ is 2, while that of $R_{Ru}(3)$ is 8. That's why the intensity of $R_{Ru}(3)$ peak is higher than $R_{Ru}(2)$ peak in the pristine $FeO_{0.7}F_{1.3}$. After charge, the intensity of $R_{Ru}(3)$ peak is lower than $R_{Ru}(2)$ peak. It could be due to the distortion of the newly formed rutile phase or the existence of other phases. A closer inspection of the result revealed a weak peak at 3.9 Å ($R_{RS}(3)$), which can be assigned to the third coordination shell ($R_{RS}(3)$) in rock salt structure. It could be concluded that the charged product is a mixture of rutile phase and rock salt phase.

2.2.2. X-Ray Diffraction (XRD) Characterization

Figure 5 shows the XRD patterns for the pristine, discharged and recharged $FeO_{0.7}F_{1.3}$/C electrodes. After discharge to 1.0 V, all the peaks of pristine rutile phase disappeared while several broad peaks were emerged. Most of them could be assigned to a rock salt phase, except one at 44.3°, which can be indexed by the (110) plane of metallic Fe. After recharge to 3.5 V, the peaks of the rock salt phase still exist with lower intensity while the (110) peak of Fe almost disappeared. Combining with EXAFS results, the newly formed rutile phase after recharge is considered to be amorphous or nanocrystalline structure.

2.2.3. Transmission Electron Microscopy (TEM) Characterization

STEM combined with SAED and EELS spectroscopy is used to investigate microstructure and morphology changes of discharged (sodiated) and charged (de-sodiated) samples. Annular dark field STEM (ADF-STEM) image of the discharged $FeO_{0.7}F_{1.3}$/C at 1.0 V is shown in **Figure 6**a. Since the ADF-STEM image contrast is sensitive to Z (atomic number), the bright contrast in Figure 6a is attributed to the presence of Fe nanoparticles with an average particle size of about 2 nm. The crystalline structure of converted phases upon full discharge can be identified from the representative SAED patterns of the discharged $FeO_{0.7}F_{1.3}$/C at 1.0 V as discussed below. HRTEM image reveals presence of nanocrystals with lattice periodicities of 0.23, 0.2 and 0.14 nm corresponding to a rock salt-like structure (Figure S4, Supporting Information). Based on the

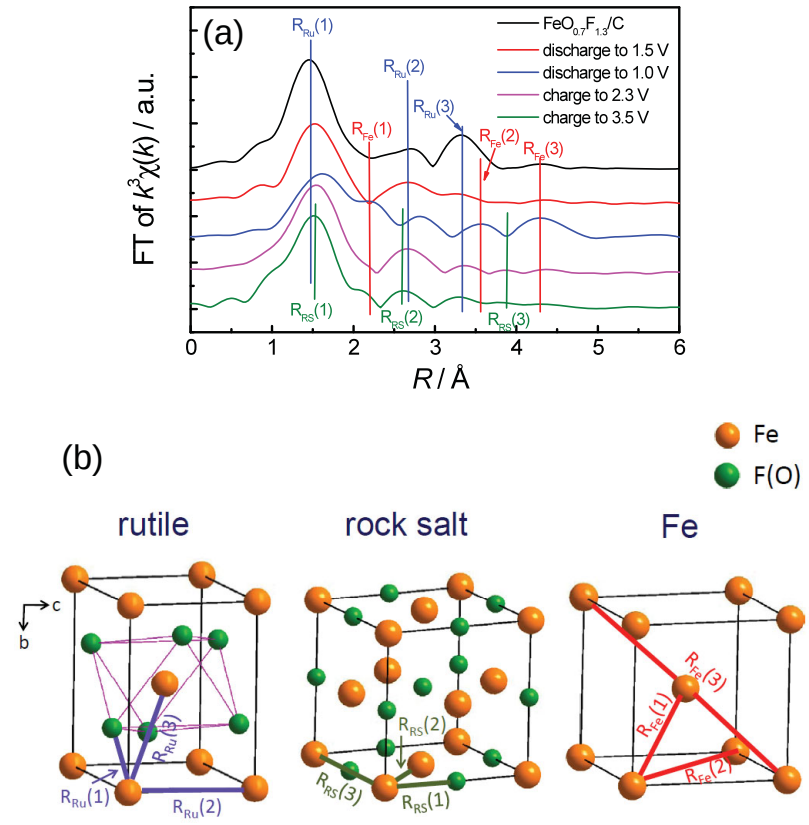

Figure 4. a) FT-EXAFS spectra of the $FeO_{0.7}F_{1.3}$/C electrodes during the initial cycle. b) Unit cells of rutile, rock salt and metal Fe structures. The nearest three coordination for Fe atoms in these structures are shown with the bold lines in different colors, which are corresponding to the peaks in FT-EXAFS spectra.

fact that the SAED patterns showed a range of intensity profiles, the sodiation process was not completely uniform. Two different areas (area A and B) with possible phases (NaF, NaFeOF, Na_2O, and Fe) are shown in **Figure 7**a. The sodiated phase did not match known fluoride phases such as orthorhombic Pnma $NaFeF_3$[12] or oxide such as trigonal (R-3m) $NaFeO_2$ or monoclinic (C2/m) $Na_{0.5}FeO_2$.[13] The intensity profiles of the sample after full sodiation (region A and B) were best associated with the superposition of NaFeOF (disordered rock salt type phase), Fe and NaF reflections. However, rock salt reflection (NaFeOF) intensities are more pronounced in the intensity profile from region A, than from region B, indicating that region A contains mostly rock salt-type phase, as opposed to the intensity profile of region B in which NaF reflection intensities are more pronounced reflecting the majority NaF phase. In both areas, Fe reflections associated with the Fe nanoparticles are also present. It should be noted that the NaF rock salt phase may not be the pure one, since some of Fe substitution into NaF phase may exist.

The ADF-STEM image of the fully charged $FeO_{0.7}F_{1.3}$/C at 3.5 V (Figure 6c) does not reveal any contrast, suggesting disappearance of metallic Fe after full charging. The corresponding SAED pattern shown in Figure 6d indicates the existence of diffuse

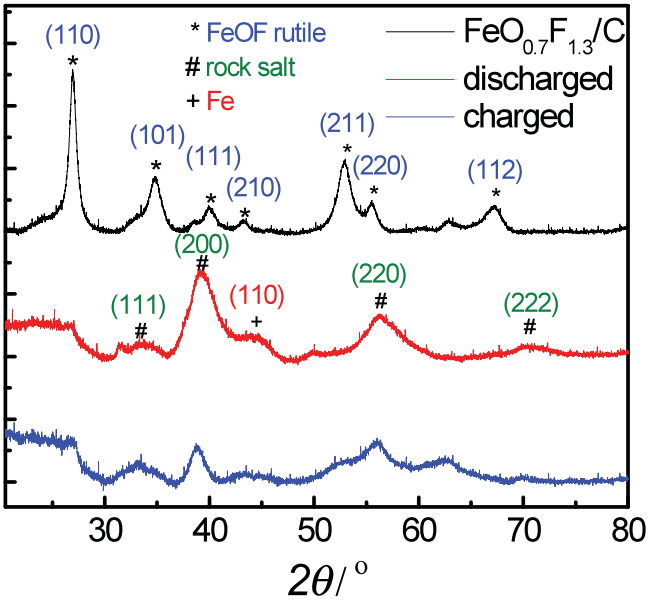

Figure 5. Ex situ X-ray diffraction patterns of the pristine $FeO_{0.7}F_{1.3}$/C (black line) and the electrodes discharged to 1.0 V (red line) and recharged to 3.5 V (blue line).

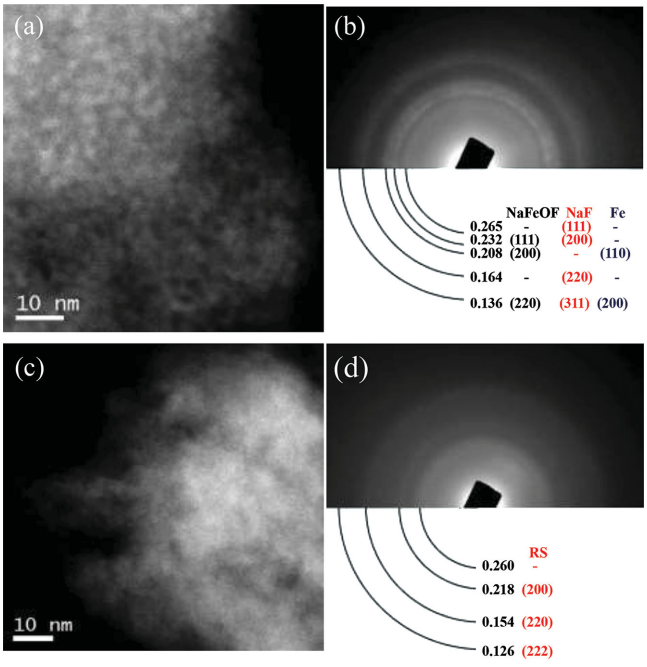

Figure 6. a) ADF-STEM image and b) SAED pattern of the discharged (i.e., sodiated) $FeO_{0.7}F_{1.3}$/C at 1.0 V; c) ADF-STEM image and d) SAED pattern of the re-charged (i.e., de-sodiated) $FeO_{0.7}F_{1.3}$/C at 3.5 V.

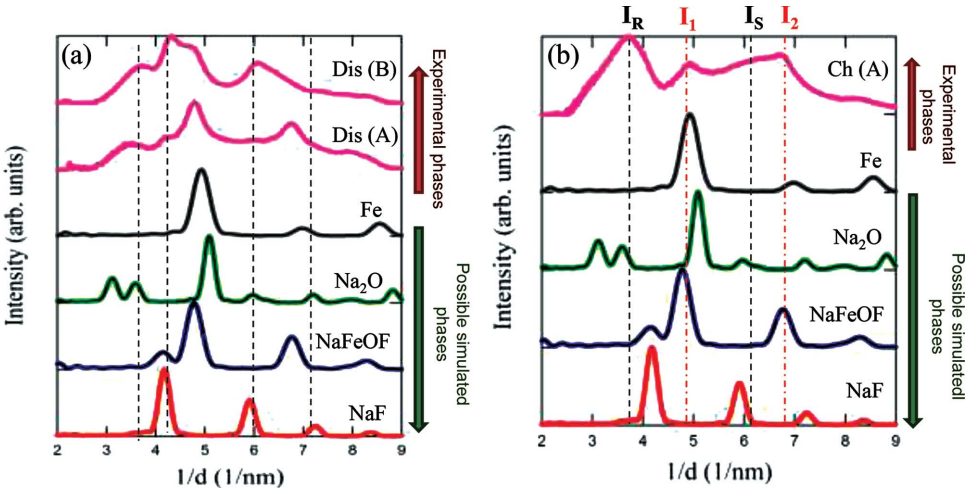

Figure 7. a) SAED intensity profiles of the discharged sample (from two different areas marked A and B) and the possible phases (NaF, NaFeOF, Na_2O, and Fe). The reflections from NaF are labeled with black dashed. b) Intensity profile of the fully charged $FeO_{0.7}F_{1.3}$/C and the possible phases (NaF, NaFeOF, Na_2O, and Fe).

rock salt-type reflections. Figure 7b shows the intensity profile of fully charged $FeO_{0.7}F_{1.3}$/C. The I1 and I2 reflections in Figure 7b (marked with red dashed lines) can be ascribed to the cubic structures (NaFeOF rock salt and Fe phases). However, metallic Fe phase can be ruled out because of the disappearance of the ADF-STEM contrast associated with Fe nanoparticles (Figure 6c). Moreover, the broad and diffuse I_R and I_S reflections in Figure S4b, Supporting Information (marked with black dashed lines), can be associated with an amorphous rutile-type structure similar to the structure observed for delithiated FeOF.[14] This indicates that the recharged $FeO_{0.7}F_{1.3}$/C after full desodiation does not reconverted back to the initial $P4_2/mnm$ rutile structure, but consists of a mixture of rock salt-type (NaFeOF) phase along with amorphous rutile-type phases. Interestingly, the fully reconverted products of $FeO_{0.7}F_{1.3}$/C (fully desodiation) show identical structures to the reconverted products of de-lithiated $FeO_{0.7}F_{1.3}$/C system.[14a]

The EELS spectra of O K- and F K- edge shown in Figure S5, Supporting Information, indicate a reversible electronic environment changes around O and F during 1st cycle. The pre-peaks of O K-edge and F K-edge are attributed to the electron transfer from O1s (F1s) into the Fe3d-O2p (Fe3d-F2p) hybridized bands. It can be seen that the intensity of pre-peaks decreased dramatically after discharge, which suggests the Fe3d-O2p (Fe3d-F2p) hybridized bands are more occupied at the discharged states, implying the reduction of Fe ions or the decomposition of $FeO_{0.7}F_{1.3}$. After recharge, the pre-peaks appeared again, indicating that the oxidation of Fe ions and the formation of Fe-O and Fe-F bonds.[15]

Taking into account all of the above results, the electrochemical reaction mechanism of $FeO_{0.7}F_{1.3}$ with Na during the first cycle is proposed as follows:

Discharge(sodiation)

$$\text{OCV} \rightarrow 1.5\text{V}: (\text{intecalation}) \quad (1)$$

$$FeO_{0.7}F_{1.3}\,(\text{rutile}) + 0.7Na^+ + 0.7e^- \rightarrow Na_{0.7}FeO_{0.7}F_{1.3}\,(\text{rutile})$$

$$1.5 \rightarrow 1.0\text{V}: (\text{conversion})$$

$$Na_{0.7}FeO_{0.7}F_{1.3}\,(\text{rutile}) + Na^+ + e^- \rightarrow 0.5Na_{1.4}FeO_{1.4}F_{0.6}\,(\text{rocksalt}) + \text{NaF}(\text{rocksalt}) + 0.5\text{Fe} \quad (2)$$

Charge(desodiation)

$$1.0 \rightarrow 2.3\text{V}: (\text{re}-\text{conversion}) \quad (3)$$

$$1.3\text{NaF}(\text{rocksalt}) + 0.5\text{Fe} \rightarrow 0.5Na_{0.6}FeF_{2.6}\,(\text{rutile}) + Na^+ + e^-$$

$$2.3 \rightarrow 3.5\text{V}: (\text{deintecalation}) \quad (4)$$

$$Na_{0.6}FeF_{2.6}\,(\text{rutile}) \rightarrow Na_{0.6-x}FeF_{2.6}\,(\text{rutile}) + xNa^+ + xe^-$$

$$Na_{1.4}FeO_{1.4}F_{0.6}\,(\text{rocksalt}) \rightarrow Na_{1.4-y}FeO_{1.4}F_{0.6}\,(\text{rocksalt}) + yNa^+ + ye^- \quad (5)$$

A schematic of the electrochemical reaction mechanisms of $FeO_{0.7}F_{1.3}$/C nanocomposite with sodium during the initial cycle is shown in **Figure 8**. From OCV to 1.5 V, an intercalation reaction occurs in the $FeO_{0.7}F_{1.3}$ rutile structure (reaction (3)) with the reduction of Fe ions. A capacity of 210 mAh g^{-1} is delivered, indicating 0.7 Na can be inserted into $FeO_{0.7}F_{1.3}$ rutile along with reduction of $Fe^{2.7+}$ to Fe^{2+}. The volume expansion of this process is estimated to be around 2.8% based on the EXAFS results. From 1.5 to 1.0 V, a conversion reaction occurs with the decomposition of the sodiated $Na_{0.7}FeO_{0.7}F_{1.3}$ rutile (reaction (5)). After discharge to 1.0 V, ultra fine Fe nanoparticles (≈2 nm) which are highly dispersed in NaF phase are formed and a newly formed rock salt phase $Na_{1.4}FeO_{1.4}F_{0.6}$ also coexists. The average valence state of Fe in the discharged products is around 1, based on the reaction (5), which agrees well with the obtained discharge capacity of

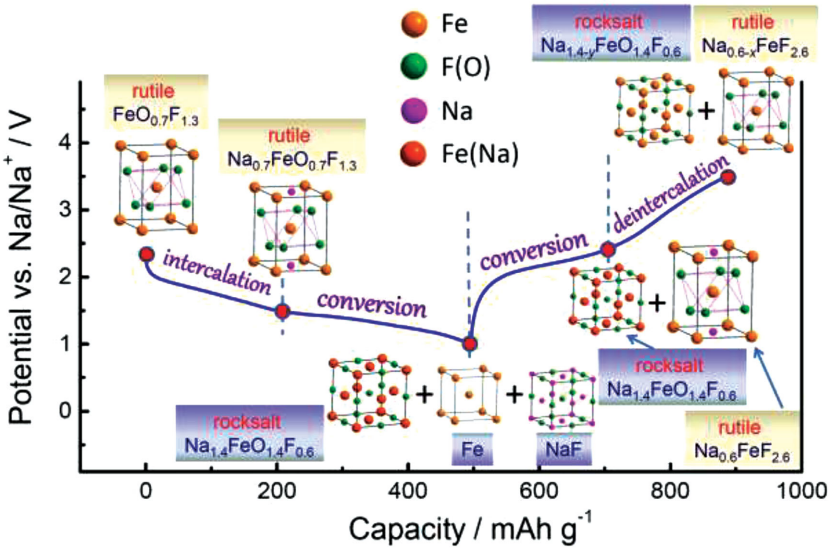

Figure 8. A schematic of the electrochemical (de)sodiation reaction mechanisms of $FeO_{0.7}F_{1.3}$/C nanocomposite during the initial cycle.

496 mAh g^{-1}. A large volume expansion in this process can be estimated, regarding the huge unit-cell volume difference between NaF rocksalt (V_{RS} = 107.85 Å^3) and $Na_{0.7}FeO_{0.7}F_{1.3}$ rutile (V_{Ru} = 68.89 Å^3). The recharge process begins with a reconversion reaction (reaction (3)). Fe nanoparticles react with NaF to form an amorphous rutile $Na_{0.6}FeF_{2.6}$ until the voltage reaches 2.3 V, associate with a large volume contraction. During further charge to 3.5 V, Na ions are deintercalated from both rutile $Na_{0.6}FeF_{2.6}$ phase (reaction (4)) and rock salt $Na_{1.4}FeO_{1.4}F_{0.6}$ phase (reaction (5)). The average volume change of the rutile and rock salt phases is around –2.3%.

Interestingly, the reaction paths of $FeO_{0.7}F_{1.3}$ with Na are quite similar as $FeO_{0.7}F_{1.3}$ in LIB system,[15] revealing that the different alkali ions size (radius: Na^+ = 0.102 nm, Li^+ = 0.076 nm) does not impact the reaction paths in $FeO_{0.7}F_{1.3}$ system. Comparing to the electrochemical performance of FeF_3 in SIBs,[8,9] $FeO_{0.7}F_{1.3}$/C nanocomposite shows higher reversible capacity and much better capacity retention. It could be due to the competition between reactions involving the rock salt and rutile components and frustration in O/F ordering in the active electrode.[14b]

3. Conclusions

In summary, the electrochemical behavior of $FeO_{0.7}F_{1.3}$/C nanocomposite in sodium ion battery system is studied for the first time. A high initial discharge capacity of 496 mAh g^{-1} and a reversible capacity of 388 mAh g^{-1} can be achieved in a voltage range of 1.0–3.5 V at 50 °C. After 50 cycles, a capacity of 360 mAh g^{-1} can still be retained, indicating superior capacity retention. Combining XAS, XRD, TEM, SAED and EELS characterization, the electrochemical reaction mechanism in the first cycle is revealed thoroughly. During discharge (sodiation) process, an intercalation reaction was followed by a conversion reaction. The discharged products are identified as a mixture of NaF, Fe nanoparticles and a newly formed rock salt phase $Na_{1.4}FeO_{1.4}F_{0.6}$. The recharge process seems reversible, commencing with a conversion reaction followed by a deintercalation reaction, but with different reaction participants. Phase separation is revealed after recharge, which is responsible for the irreversible capacity loss and the voltage hysteresis during the first cycle. On the other hand, the phase separation may be beneficial for stabilizing the (de)sodiation reactions during the subsequent cycles, since the competition between reactions involving the rock salt and rutile components are favorable to enhancing the cyclability of nanosized composite electrode. It should be noted that the $FeO_{0.7}F_{1.3}$/C nanocomposite has similar working potential and capacity comparing with sodium-sulfur and sodium-air systems, but much better cycle performance. These results might open new opportunities to develop high capacity cathode materials for sodium ion batteries.

4. Experimental Section

Material Synthesis and Electrochemical Test: The $FeO_{0.7}F_{1.3}$ nanoparticles were synthesized via a solution process involving reacting iron metal with a fluorosilicic acid aqueous solution. The resulting $FeSiF_6{\cdot}6H_2O$ precursor was then annealed in air between 50 and 300 °C. The synthesis details were reported in a previous literature.[10a] $FeO_{0.7}F_{1.3}$/C nanocomposites were prepared by high-energy ball milling the as-prepared $FeO_{0.7}F_{1.3}$ nanoparticles with 15 wt% activated carbon black for 1 hour in a helium atmosphere (weight % of carbon in the nanocomposite = 15%). The electrodes were fabricated using the Bellcore developed process consisting of mixing the active materials with poly (vinylidene fluoride-cohexafluoropropylene) (Kynar 2801, Elf Atochem), carbon black (super P, MMM), and dibutyl phthalate (Aldrich). The resulting electrodes typically consisted of 57% active material. The experimental details on electrode preparation can be found in a previous literature.[10a] The specific capacity and current density reported in this paper are based on the active material ($FeO_{0.7}F_{1.3}$) in the nanocomposite. 1.0 M $NaClO_4$ in ethylene carbonate (EC) and dimethyl carbonate (DMC) with a volume ratio of 1:1 was used as the electrolyte. High purity sodium foil was used as the counter electrode. The 2032-type coin cells were assembled in an argon-filled glove box for electrochemical tests. It is known that the activation barrier to trigger the oxidation and reduction reactions for the conversion-type electrode material is high and their kinetics is poor. The full discharge capacity can only be obtained at a C/40 rate or lower when samples were tested at room temperature. In order to complete the in situ X-ray experiments within limited beamtime available and the cycle life test within reasonable time frame, the $FeO_{0.7}F_{1.3}$/C-Na cells were cycled at 50 °C.

X-Ray Diffraction and Absorption Spectroscopy: Ex situ X-ray diffraction patterns were collected at beamline X14A of the National Synchrotron Light Source (NSLS) at Brookhaven National Laboratory (BNL) using a linear position sensitive silicon detector. The wavelength used was 0.7787 Å. In situ Fe K-edge X-ray absorption spectroscopy (XAS) spectra were measured in the transmission mode at beamline X18A of NSLS. Energy calibration was carried out using the reference spectrum of Fe

metal foil (Fe K-edge = 7112 eV) which was simultaneously collected during each scan and used to calibrate the energy position during data process. The X-ray absorption near edge structure (XANES) and extended X-ray absorption fine structure (EXAFS) data were analyzed using the ATHENA software package.[16] The AUTOBK code was used to normalize the absorption coefficient, and separate the EXAFS signal, $\chi(k)$, from the isolated atom-absorption background. The extracted EXAFS signal, $\chi(k)$, was weighted by k^3 to emphasize the high-energy oscillations and then Fourier-transformed in a k range from 3.2 to 10.6 Å^{-1} using a hanning window with a window sill (Δk) of 1.0 Å^{-1}, thereby obtaining magnitude plots of the EXAFS spectra in R-space (Å). The Fourier-transformed peaks were not phase corrected, and thus the actual bond lengths are approximately 0.3–0.5 Å longer.

Transmission Electron Microscopy Experiments: For TEM characterization, the electrochemical cells were disassembled in a helium-filled glove box and the extracted powder from the positive electrode was rinsed in DMC. The electrode powder was then dispersed in DMC and a few drops placed on a TEM lacy carbon film supported on a copper grid. The TEM samples were loaded on a vacuum transfer holder and transferred to the TEM without exposure to air. Selected area electron diffraction (SAED) pattern, annular dark field scanning transmission electron microscopy (ADF-STEM), and electron energy loss spectroscopy (EELS) were recorded at 197 KV with a JEOL-2010F microscope equipped with a Gatan imaging filter (GIF) spectrometer. The energy resolution of the EELS spectra measured from the full width at half magnitude (FWHM) of the zero-loss peak (ZLP) was 0.9 eV. In addition, a collection angle (b) of 20 mrad and an illumination convergence angle (a) of 10 mrad were used for the EELS spectra acquisition. Process diffraction program was utilized for obtaining SAED intensity profiles by first taking the rotational average followed by background removal.[17] In addition, JEMS software was used for simulating SAED intensity profiles of nano-sized particles in the 2–5 nm range. These were obtained ab initio by calculating the pair distribution function and solving the Debye equation.[18]

Supporting Information

Supporting Information is available from the Wiley Online Library or from the author.

Acknowledgements

The work was supported by the Northeastern Center for Chemical Energy Storage, an Energy Frontier Research Center funded by the US Department of Energy, Office of Science, Office of Basic Energy Sciences under Contract Number DE-SC0001294. Yong-Ning Zhou and Xiqian Yu were supported by the US Department of Energy, the Assistant Secretary for Energy Efficiency and Renewable Energy, Office of Vehicle Technologies under Contract Number DE-AC02–98CH10886. The use of the National Synchrotron Light Source was supported by the US Department of Energy, Office of Science, Office of Basic Energy Sciences, under Contract No. DEAC02–98CH10886. K.W. Nam was supported by the Dongguk University Research Fund of 2014.

Received: September 17, 2014
Revised: October 21, 2014
Published online: November 20, 2014

[1] M. D. Slater, D. Kim, E. Lee, C. S. Johnson, *Adv. Funct. Mater.* **2013**, *23*, 947.
[2] a) V. Palomares, P. Serras, I. Villaluenga, K. B. Hueso, J. Carretero-Gonzalez, T. Rojo, *Energy Environ. Sci.* **2012**, *5*, 5884; b) S. W. Kim, D. H. Seo, X. H. Ma, G. Ceder, K. Kang, *Adv. Energy Mater.* **2012**, *2*, 710.
[3] a) N. Yabuuchi, M. Kajiyama, J. Iwatate, H. Nishikawa, S. Hitomi, R. Okuyama, R. Usui, Y. Yamada, S. Komaba, *Nat. Mater.* **2012**, *11*, 512; b) S. P. Ong, V. L. Chevrier, G. Hautier, A. Jain, C. Moore, S. Kim, X. H. Ma, G. Ceder, *Energy Environ. Sci.* **2011**, *4*, 3680; c) R. Tripathi, T. N. Ramesh, B. L. Ellis, L. F. Nazar, *Angew. Chem. Int. Ed.* **2010**, *49*, 8738; d) M. Sathiya, K. Hemalatha, K. Ramesha, J. M. Tarascon, A. S. Prakash, *Chem. Mater.* **2012**, *24*, 1846.
[4] a) H. Li, G. Richter, J. Maier, *Adv. Mater.* **2003**, *15*, 736; b) F. Badway, N. Pereira, F. Cosandey, G. G. Amatucci, *J. Electrochem. Soc.* **2003**, *150*, A1209; c) F. Badway, F. Cosandey, N. Pereira, G. G. Amatucci, *J. Electrochem. Soc.* **2003**, *150*, A1318; d) F. Badway, A. N. Mansour, N. Pereira, J. F. Al-Sharab, F. Cosandey, I. Plitz, G. G. Amatucci, *Chem. Mater.* **2007**, *19*, 4129; e) F. Wang, H. C. Yu, M. H. Chen, L. J. Wu, N. Pereira, K. Thornton, A. Van der Ven, Y. M. Zhu, G. G. Amatucci, J. Graetz, *Nat.Commun.* **2012**, *3*, 1201; f) Y. H. Cui, M. Z. Xue, Y. N. Zhou, S. M. Peng, X. L. Wang, Z. W. Fu, *Electrochim. Acta* **2011**, *56*, 2328.
[5] a) Y. N. Zhou, H. Zhang, M. Z. Xue, C. L. Wu, X. J. Wu, Z. W. Fu, *J. Power Sources* **2006**, *162*, 1373; b) Y. Y. Hu, Z. G. Liu, K. W. Nam, O. J. Borkiewicz, J. Cheng, X. Hua, M. T. Dunstan, X. Q. Yu, K. M. Wiaderek, L. S. Du, K. W. Chapman, P. J. Chupas, X. Q. Yang, C. P. Grey, *Nat. Mater.* **2013**, *12*, 1130; c) H. Li, P. Balaya, J. Maier, *J. Electrochem. Soc.* **2004**, *151*, A1878; d) S. Mitra, P. Poizot, A. Finke, J. M. Tarascon, *Adv. Funct. Mater.* **2006**, *16*, 2281; e) K. M. Shaju, F. Jiao, A. Debart, P. G. Bruce, *Phys. Chem. Chem. Phys.* **2007**, *9*, 1837; f) O. Delmer, P. Balaya, L. Kienle, J. Maier, *Adv. Mater.* **2008**, *20*, 501; g) P. Poizot, S. Laruelle, S. Grugeon, L. Dupont, J. M. Tarascon, *Nature* **2000**, *407*, 496; h) C. Z. Yuan, H. B. Wu, Y. Xie, X. W. Lou, *Angew. Chem. Int. Ed.* **2014**, *53*, 1488; i) J. Y. Wang, N. L. Yang, H. J. Tang, Z. H. Dong, Q. Jin, M. Yang, D. Kisailus, H. J. Zhao, Z. Y. Tang, D. Wang, *Angew. Chem. Int. Ed.* **2013**, *52*, 6417.
[6] a) N. Pereira, L. C. Klein, G. G. Amatucci, *J. Electrochem. Soc.* **2002**, *149*, A262; b) Y. N. Zhou, C. Liu, H. J. Chen, L. Zhang, W. J. Li, Z. W. Fu, *Electrochim. Acta* **2011**, *56*, 5532; c) N. Pereira, L. Dupont, J. M. Tarascon, L. C. Klein, G. G. Amatucci, *J. Electrochem. Soc.* **2003**, *150*, A1273; d) B. Das, M. V. Reddy, G. V. S. Rao, B. V. R. Chowdari, *J. Mater. Chem.* **2012**, *22*, 17505.
[7] F. Klein, B. Jache, A. Bhide, P. Adelhelm, *Phys. Chem. Chem. Phys.* **2013**, *15*, 15876.
[8] M. Nishijima, I. D. Gocheva, S. Okada, T. Doi, J. Yamaki, T. Nishida, *J. Power Sources* **2009**, *190*, 558.
[9] C. L. Li, C. L. Yin, L. Gu, R. E. Dinnebier, X. K. Mu, P. A. van Aken, J. Maier, *J. Am. Chem. Soc.* **2013**, *135*, 11425.
[10] a) N. Pereira, F. Badway, M. Wartelsky, S. Gunn, G. G. Amatucci, *J. Electrochem. Soc.* **2009**, *156*, A407; b) W. Tong, W. S. Yoon, G. G. Amatucci, *J. Power Sources* **2010**, *195*, 6831; c) W. Tong, W. S. Yoon, N. M. Hagh, G. G. Amatucci, *Chem. Mater.* **2009**, *21*, 2139; d) W. Tong, G. G. Amatucci, *Electrochem. Solid-State Lett.* **2009**, *12*, A219.
[11] F. J. Brink, R. L. Whiters, L. Noren, *J. Solid State Chem.* **2001**, *161*, 31.
[12] A. Kitajou, H. Komatsu, K. Chihara, I. D. Gocheva, S. Okada, J. Yamaki, *J. Power Sources* **2012**, *198*, 389.
[13] Y. Takeda, K. Nakahara, M. Nishijima, N. Imanishi, O. Yamamoto, M. Takano, R. Kanno, *Mater. Res. Bull.* **1994**, *29*, 659.
[14] a) M. Sina, K. W. Nam, D. Su, N. Pereira, X. Q. Yang, G. G. Amatucci, F. Cosandey, *J. Mater. Chem. A* **2013**, *1*, 11629; b) K. M. Wiaderek, O. J. Borkiewicz, E. Castillo-Martinez, R. Robert, N. Pereira, G. G. Amatucci, C. P. Grey, P. J. Chupas, K. W. Chapman, *J. Am. Chem. Soc.* **2013**, *135*, 4070.
[15] F. Cosandey, D. Su, M. Sina, N. Pereira, G. G. Amatucci, *Micron* **2012**, *43*, 22.
[16] B. Ravel, M. Newville, *J. Synchrotron. Radiat.* **2005**, *12*, 537.
[17] J. L. Labar, M. Adamik, B. P. Barna, Z. Czigany, Z. Fogarassy, Z. E. Horvath, O. Geszti, F. Misjak, J. Morgiel, G. Radnoczi, G. Safran, L. Szekely, T. Szuts, *Microsc. Microanal.* **2012**, *18*, 406.
[18] JEMS Website, http://cimewww.epfl.ch/people/stadelmann/jemswebsite/jems.html (accessed November 2014).